Journal of
Materials in Life Sciences

Vol. 4 No. 1 (2025)

Full Paper

Polynomial-Optimized Calcination of TiO_2-Based Photoanodes for Enhanced Photocurrent in Solar Hydrogen Production: Integrating Data Science with Functional Design

Siti Nur Umairah Shikh Mohd Fauzi[a], Khairul Rijal Razali[a], Siti Salwa Alias[b,c], Nik Ahmad Nizam Nik Malek[b,d], Taufiq Khairi Ahmad Khairuddin[e], Susilawati Toemen[a], Habib Ullah[f], Juan Matmin[a,b]*

[a]Department of Chemistry, Faculty of Science, Universiti Teknologi Malaysia, 81310 UTM Johor Bahru, Johor, Malaysia.
[b]Centre for Sustainable Nanomaterials, Universiti Teknologi Malaysia, 81310 UTM Johor Bahru, Johor, Malaysia.
[c]Department of Physics, Faculty of Science, Universiti Teknologi Malaysia, 81310 UTM Johor Bahru, Johor, Malaysia.
[d]Department of Biosciences, Faculty of Science, Universiti Teknologi Malaysia, 81310 UTM Johor Bahru, Johor, Malaysia.
[e]Department of Mathematical Sciences, Faculty of Science, Universiti Teknologi Malaysia, 81310 UTM Johor Bahru, Johor, Malaysia.
[f]College of Engineering Mathematics and Physical Sciences, University of Exeter, Penryn Campus, Cornwall TR10 9FE, UK.

Article history
Received
18 April 2025
Revised
12 May 2025
Accepted
26 May 2025
Published online
31 May 2025

*Corresponding author
juanmatmin@utm.my

Abstract

The calcination temperature of metal oxide semiconductors plays a pivotal role in dictating their crystallinity, phase purity, and charge transport behavior, all of which are critical to enhancing photoelectrochemical (PEC) water splitting. In this study, we apply a fifth-order polynomial curve fitting model to analyze and optimize the calcination temperature of various n-type semiconductors, ultimately identifying 550°C as the first-layer calcination temperature for titanium dioxide (TiO_2) photoanodes. Based on this data-driven insight, bimetallic oxide composites of ZnO/TiO_2 (1:2) and MnO_2/TiO_2 (1:2) were synthesized via solid-state mixing followed by thermal treatment at the polynomial-predicted temperature. X-ray diffraction (XRD) analyses revealed the formation of tetragonal anatase TiO_2, hexagonal wurtzite ZnO, and β-MnO_2 crystalline phases in their respective composites. Structural refinement revealed an increase in crystallite size and d-spacing shifts, indicative of heterojunction formation. Photoelectrochemical measurements under simulated sunlight revealed that MnO_2/TiO_2 (1:2) exhibited the highest photocurrent density (0.02052 A cm^{-2}), outperforming pristine TiO_2 and ZnO/TiO_2 (1:2) composites. Electrochemical impedance spectroscopy (EIS) further demonstrated a reduced charge transfer resistance in MnO_2/TiO_2 (9.76 Ω), supporting its superior PEC performance. This work demonstrates a successful integration of predictive modelling with materials synthesis, offering a rational and reproducible pathway for optimizing thermally treated photoanodes for solar-driven hydrogen generation.

Keywords titanium dioxide, polynomial fitting, bimetallic photoanodes, hydrogen production, water splitting

1.0 INTRODUCTION

The rising demand for sustainable energy technologies has prompted intensive exploration of hydrogen as a clean and efficient energy carrier. Among various hydrogen production methods, photoelectrochemical (PEC) water splitting represents a promising solar-to-fuel conversion strategy, offering direct utilization of solar energy to generate hydrogen from water without carbon emissions. Notably, titanium dioxide (TiO_2) has long been a material of choice in PEC applications due to its low cost, photochemical stability, and favorable conduction and valence band positions for water redox reactions (Jang et al., 2016). However, its wide bandgap and fast recombination of photoinduced electron–hole pairs limit its solar energy utilization and overall, PEC performance (Xu et al., 2021).

To overcome these intrinsic limitations, strategies such as heterojunction formation, surface sensitization, and doping have been widely employed. In particular, the incorporation of transition metal co-catalysts such as Ru, Co, and Ni has shown substantial improvements in hydrogen generation and interfacial conductivity when coupled with TiO_2, primarily by promoting charge separation and enhancing the kinetics of the hydrogen evolution reaction (Thabet et al., 2024). Furthermore, insights from ultrafast transient absorption spectroscopy have confirmed that the recombination dynamics in TiO_2 are strongly phase dependent. Particularly, anatase TiO_2, with fewer surface defects, exhibits lower charge recombination rates than its rutile counterpart, making it more suitable for PEC applications (Jiang et al., 2016).

Notably, a key but often under-optimized factor in determining TiO_2's performance is its calcination temperature. Calcination affects not only the crystallinity and phase purity of TiO_2 but also its grain growth, surface area, and defect structure. These parameters directly influence its photoactivity, electronic conductivity, and light absorption characteristics (Wang et al., 2021). Furthermore, inappropriate calcination temperatures on TiO_2 may result in unwanted grain growth, which hinders charge mobility and surface reactivity. Although numerous studies have demonstrated the effects of thermal treatment on TiO_2 photocatalysts, the selection of calcination temperature is often based on trial-and-error or heuristic approaches, lacking a rigorous predictive framework.

In response to this challenge, we propose a data-guided strategy to rationally determine the ideal calcination temperature for TiO_2-based materials. By applying a fifth-order polynomial curve fitting to a large dataset of n-type semiconductor photoanodes (n = 3402), correlating calcination temperature with bandgap values, a calcination temperature of 550°C for TiO_2 was identified as a moderate first-layer calcination temperature for maximizing bandgap-dependent photocatalytic behavior in TiO_2. A fifth-order polynomial model was chosen after systematic testing of various polynomial degrees to best capture the complex, nonlinear relationship between calcination temperature and photocurrent density. Lower-order models (e.g., quadratic or cubic) could not accurately represent the observed data trends, while higher-order models led to overfitting and poor predictive reliability. This modeling-driven insight served as the foundation for the synthesis of TiO_2-based bimetallic oxide heterostructures incorporating ZnO and MnO_2, selected from group 12 and group 7 transition metal oxides, respectively. Likewise, both ZnO and MnO_2 are known for their potential to enhance visible-light absorption and charge carrier dynamics when interfaced with TiO_2.

The novelty of this study lies in integrating polynomial modelling with experimental synthesis to rationally design photoanodes, enabling a predictive and reproducible approach to calcination. This process has traditionally been experimental. Unlike conventional heterostructure designs, this work systematically studied the influence of d-group metal oxides on TiO_2 crystallite structure, d-spacing, and interfacial charge transport. Moreover, by evaluating the PEC performance of these materials in terms of photocurrent density and charge transfer resistance, the study reveals fundamental structure–function relationships and offers a scalable framework for engineering thermally optimized photoanodes for efficient solar hydrogen production. This approach demonstrates the value of combining statistical modeling with materials chemistry to tailor photoanode properties and advance solar hydrogen production technologies.

2.0 METHODOLOGY

The study adopted a three-stage approach, starting with computational modeling to optimize TiO_2 calcination conditions. A Random Forest regression model was implemented using Python's scikit-learn (v1.2.2) to identify key predictors. Variable importance was quantified using IncNodePurity and the percentage increase in mean squared error (%IncMSE) (i.e., indicators of how much each variable contributes to model accuracy and decision-tree purity, respectively). This study utilized secondary data originally collected by Oral et al. (2022) for different research purposes. The dataset comprises detailed records of a PEC experiment involving an n-type semiconductor, including electrode materials, synthesis methods, irradiation conditions, and electrolyte solution properties. Additionally, polynomial curve fitting was conducted in MATLAB using the *polyfit* function (Equation 2.1) to determine the coefficients of a polynomial model that best fits a given dataset via the least squares method.

$$p = polyfit(x, y, n) \quad \text{(Equation 2.1)}$$

where, p is the vector representing the coefficients of the best-fitted polynomial in descending power, x is the vector representing the independent variable, y is the vector representing the dependent variable, and n is the vector representing the degree of the polynomial.

After the coefficients were obtained, the *polyval* command (Equation 2.2) was employed to evaluate the predicted values of the polynomial or analyse trends at specified points.

$$y = polyval(p, xq) \quad \text{(Equation 2.2)}$$

Coefficient of determination (R^2) (Equation 2.3) and residual sum of squares (SSE) were employed as a performance indicator. R^2 ranges between 0 and 1 measures how well a regression model fits the data and predicts future outcomes, where higher values indicate a better fit.

$$R^2 = \frac{\sum(\hat{y}_i - \overline{y})^2}{\sum(y_i - \overline{y})^2} \quad \text{(Equation 2.3)}$$

where $\hat{y}_i$ is the predicted value, $\overline{y}$ is the mean of the actual value, and y_i is the actual value.

SSE (Equation 2.4) quantifies the overall variation or error in a regression model by measuring how much the predicted values, $\hat{y}_i$ differ from the actual values, y_i, squared and summed across all data points. A lower SSE indicates that the model's predictions closely match the actual data, suggesting a more accurate and reliable model.

$$SSE = \sum(y_i - \hat{y}_i)^2 \quad \text{(Equation 2.4)}$$

The optimal calcination temperature was determined using nth-order polynomial curve fitting (n=1, 2, 3, 4, 5, 6) performed in MATLAB R2023a with the *polyfit* function, and model accuracy was verified by a coefficient of determination (R^2) of 0.94. For material synthesis, metal oxides were prepared via a modified sol-gel method. Anatase TiO_2 (99.9%, Sigma-Aldrich) was dispersed in ethanol using a Branson 5800 ultrasonic bath (40 kHz, 30 min), then mixed with either ZnO or MnO_2 in 1:2 and 1:4 molar ratios. The mixtures were magnetically stirred (IKA RCT, 500 rpm, 3 h), centrifuged (Eppendorf 5430, 4000 rpm, 10 min), and dried (Memmert UF110 oven, 110°C, 12 h) before calcination in a Nabertherm furnace (550°C, 3 h, 5°C/min ramp rate). X-ray diffraction (XRD) characterization was performed with a Rigaku diffractometer (Cu-Kα radiation, λ = 1.5406 Å, 40 kV, 40 mA). Crystallographic analysis employed Bragg's Law for d-spacing calculation and the Debye-Scherrer equation (with Scherrer constant K = 0.94) for crystallite size determination from peak broadening. Phase identification was achieved by matching Miller indices to JCPDS reference patterns (TiO_2 PDF #21-1272, ZnO PDF #36-1451).

The photocurrent performance was evaluated using a Gamry Interface 1000 potentiostat in a three-electrode configuration consisting of photoanodes as working electrodes (with illuminated area of 1cm^2), Ag/AgCl (3 M KCl) as reference electrode, and platinum wire as counter electrode. The tests were conducted at a scan rate of 100 mVs^{-1}. Working electrodes were prepared by pressing 100 mg of catalyst material onto a carbon-coated glass substrate (1 cm^2 area). Linear sweep voltammetry (LSV) was conducted in 0.5 M Na_2SO_4 electrolyte (pH 7) at 10 mV/s scan rate under AM 1.5 G illumination (PEC-L01 solar simulator, 100 mW/cm^2). Potentials were converted to the Reversible Hydrogen Electrode (RHE) scale using the Nernst equation, accounting for the Ag/AgCl reference electrode potential (+0.210 V vs NHE at 25°C). The applied potential was varied from 0.0 V to 1.8 V vs. RHE, in the dark and under 2 h of illumination. Electrochemical Impedance Spectroscopy (EIS) is a technique used to study the electrical behavior of materials by applying an alternating voltage and measuring the current response across a range of frequencies. In this work, EIS was applied to analyze the electrochemical properties of synthesized metal oxides. The impedance data—real (Z') and imaginary (Z'') components from the Nyquist plot, along with frequency data from the Bode plot—were fitted to an equivalent circuit model using Z_{Sim} 3.20 to represent the system's physical processes. From the Nyquist plot, the charge transfer resistance (R_{ct}) was obtained by measuring the diameter of the semicircle, offering insights into the electron transfer kinetics at the electrode–electrolyte interface. The overall research scheme is presented in Figure 1.

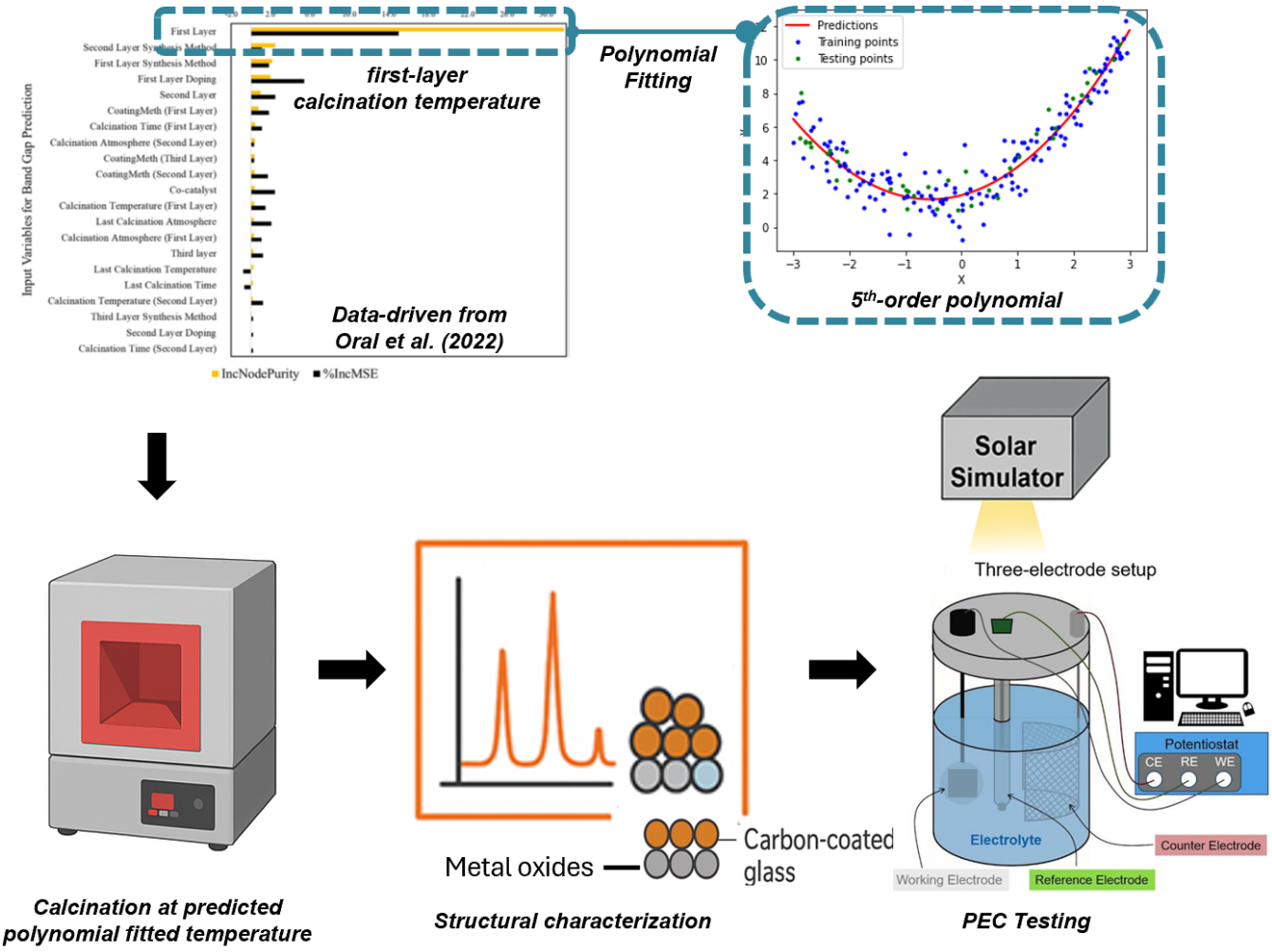

Figure 1 Operational research scheme for polynomial-optimized calcination of TiO_2-based photoanodes.

3.0 RESULTS AND DISCUSSION

Our study builds upon the foundational work of Oral et al. (2022), whose Random Forest analysis identified first-layer calcination temperature as the most statistically significant predictor of band gap energy, as evidenced by its dominant percentage increase in mean squared error (%IncMSE) among all continuous variables. We utilized their comprehensive dataset of 10,559 experimental entries spanning thirty photoelectrode materials, applying rigorous data cleaning protocols to ensure analytical reliability. This process involved systematically removing entries with missing values for either first-layer calcination temperature or band gap measurements, resulting in a refined dataset of 3,402 high-quality entries representing seventeen well-characterized n-type semiconductors. To optimize our analysis, we prioritized five frequently studied materials (TiO_2, FeO, BiVO, WO, and TaN), which collectively constituted 81.42% of the dataset. We grouped eleven less-represented electrode types as "others." Following established practices for reducing analytical noise, we excluded Niobium(II) oxide (NbO) due to its potential to introduce confounding effects. This strategic approach to data curation enabled focused investigation of structure-property relationships while controlling for variability in photoelectrochemical performance metrics.

To systematically investigate the relationship between first-layer calcination temperature and band gap in n-type semiconductors, we employed a multi-stage analytical approach (Figure 2). Data standardization was first performed by assigning representative values to each electrode type, ensuring consistency across the dataset. Initial exploratory analysis, conducted through scatter plotting, revealed no clear linear correlation, prompting the use of more sophisticated modeling techniques (Figure 2(a)). A fifth-order polynomial regression was implemented to capture potential nonlinear behavior, selected for its ability to model complex relationships while accommodating the available data points. The model, developed using MATLAB's curve-fitting tools, demonstrated strong predictive capabilities both within and beyond the experimental temperature range.

Interestingly, the model can predict values of the dependent variable (band gap) for independent variable values (calcination temperature) that fall within or outside the range of the existing data using Equation 3.1.

$$f(x) = -2.6976 \times 10^{-9}x^5 + 8.2587 \times 10^{-6}x^{-4} - 0.0099275x^3 \quad \text{(Equation 3.1)}$$

As shown in Figure 2(b), the polynomial analysis revealed three distinct temperature-dependent regimes: a stable low-temperature region (<625 °C), a sharp transitional phase (625–850 °C) characterized by rapid changes in band gap, and a high-temperature degradation region (>850 °C). Model validation demonstrated an excellent fit (R^2 = 0.9999) and low prediction error (SSE = 2.7199), although potential overfitting was observed in areas with sparse data. When applied practically, the model successfully predicted a calcination temperature of 550 °C for anatase TiO_2 with a 3.3 eV band gap, consistent with reported values in the literature. This approach offers valuable insights into the temperature dependence of band gap behavior, while also highlighting the need for alternative modelling techniques to overcome the limitations of polynomial fitting in future studies.

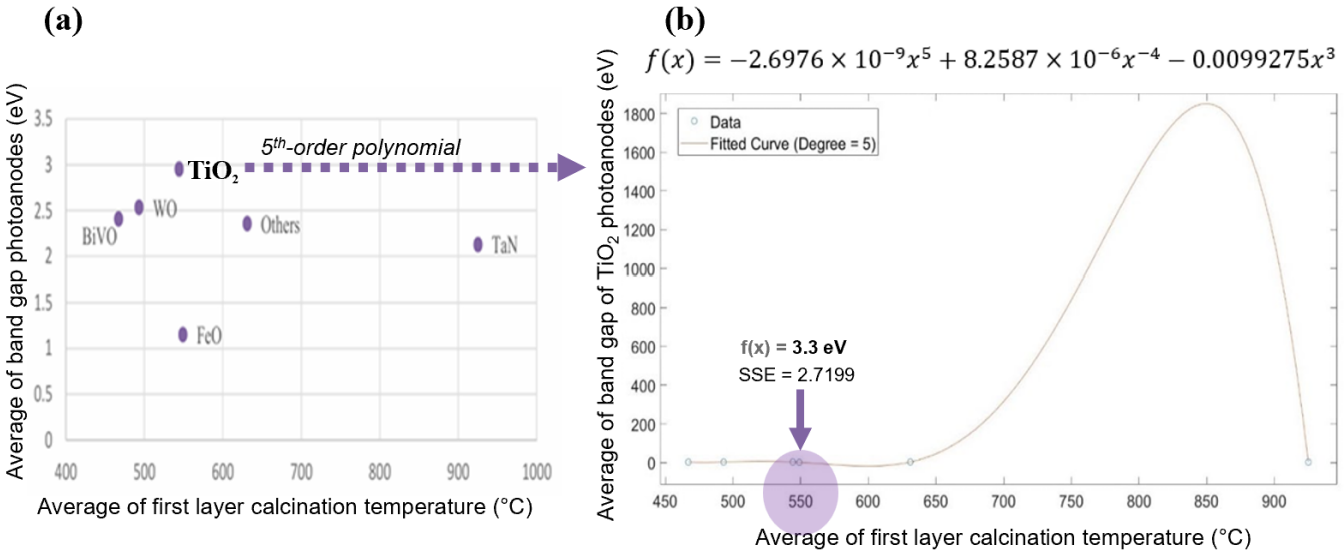

Figure 2 Polynomial analysis using (a) different types of photoanodes, (b) 5-th order polynomial fit on TiO_2-based photoanode

Figure 3 displays the XRD patterns of TiO_2, ZnO/TiO_2 (1:2), and MnO_2/TiO_2 (1:2) composites. A prominent peak corresponding to the (110) diffraction plane is evident in all samples, indicating that the anatase TiO_2 phase is retained in both ZnO/TiO_2 (1:2) and MnO_2/TiO_2 (1:2) composites. For the ZnO/TiO_2 (1:2) sample, the reflection peaks at 2θ = 31.70°, 34.36°, 36.18°, 47.98°, 56.52°, 62.72°, and 67.88°, which correspond to the (100), (002), (101), (102), (110), (103), and (112) planes, confirm the presence of hexagonal wurtzite ZnO (Sun et al, 2020). In Figure 3(c), the peaks observed at 2θ = 28.66°, 37.34°, 40.98°, 42.80°, 56.66°, and 59.36°, corresponding to the (110), (101), (200), (111), (211), (220), and (301) planes, confirm the presence of β-MnO_2 in the MnO_2/TiO_2 (1:2) composite, in agreement with previously reported data (Alonizan et al., 2018).

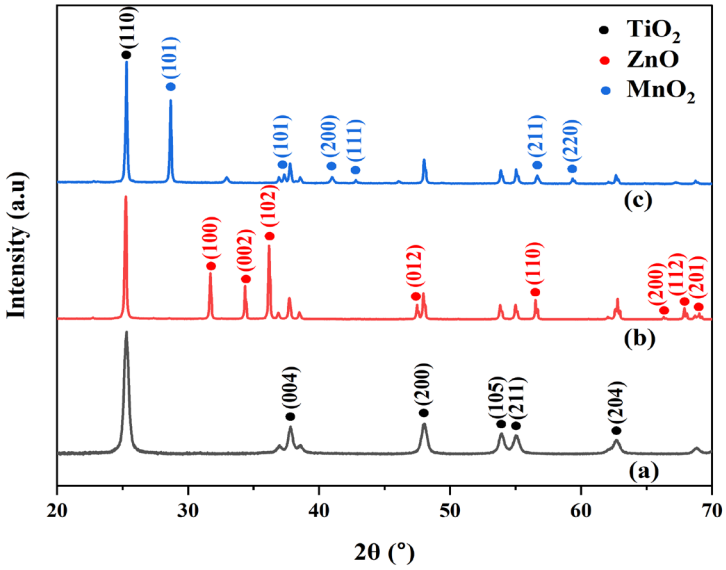

Figure 3 XRD analysis of (a) TiO_2, (b) ZnO/TiO_2 (1:2) and (c) MnO_2/TiO_2 (1:2).

As shown in Table 1, the crystallite size of the samples increases in the order: TiO_2 (17.53 nm) < ZnO/TiO_2 (1:2) (49.70 nm) < MnO_2/TiO_2 (1:2) (50.72 nm). This trend aligns with periodic trends in ionic radii, where elements from earlier groups generally have larger ionic sizes. Since Mn belongs to Group 7 and Zn to Group 12, the slightly larger crystallite size of MnO_2/TiO_2 may be attributed to the larger ionic radii of Mn^{2+}. For the (110) plane, TiO_2 and ZnO/TiO_2 (1:2) share a similar d-spacing of 3.5257 Å, indicating that ZnO incorporation does not significantly disrupt the TiO_2 lattice structure. In contrast, MnO_2/TiO_2 (1:2) shows a slightly reduced d-spacing of 3.5174 Å. This small difference corresponds to a 0.06° shift in 2θ (from 25.30° to 25.24°), suggesting minor lattice distortions, likely due to the formation of surface defects. These defects may enhance photoelectrocatalytic activity by providing additional active edge sites (Lai et al., 2023).

Table 1 The crystal structure characteristics of TiO_2, ZnO/TiO_2 (1:2) and MnO_2/TiO_2 (1:2).

Sample	2θ (°)		d-spacing (Å)	FWHM (°)	Crystallize size (nm)	Average Crystallize Size (nm)
TiO_2	25.24	(110)	3.5257	0.44974	18.10	17.53
	37.83	(004)	2.3763	0.49988	16.80	
	48.03	(200)	1.8927	0.49169	17.69	
ZnO/TiO_2 (1:2)	25.24	(110)	3.5257	0.16967	47.98	49.70
	31.70*	(100)	2.8204	0.17153	48.14	
	36.18*	(101)	2.4808	0.15772	52.99	
MnO_2/TiO_2 (1:2)	25.30	(110)	3.5174	0.16847	48.33	50.72
	28.66#	(101)	3.1122	0.15421	53.17	
	48.02	(200)	1.8931	0.17167	50.66	

*indicated for ZnO, # indicated for MnO_2

For the hydrogen evolution reaction (HER) to proceed efficiently, the applied potential should ideally be more positive than the standard hydrogen reduction potential (0 V vs. RHE) (Manna et al., 2024). In this study, a photocurrent density measured at 0.61 V vs. RHE is used as a performance benchmark. As shown in Figure 4, the photocurrent densities were evaluated both in the dark and after 2 h of illumination. The photoresponse at 0.61 V vs. RHE reveals the ranking of the photoanodes' activity as follows: MnO_2/TiO_2 (1:2) > TiO_2 > ZnO/TiO_2 (1:2). All photoanodes demonstrated increased photocurrent upon light exposure, with MnO_2/TiO_2 achieving the highest photocurrent density of 0.02052 A/cm², indicating

superior charge separation and visible light harvesting efficiency. In contrast, ZnO/TiO_2 (1:2) showed the least photocurrent enhancement, suggesting limited synergistic interaction between ZnO and TiO_2. This performance is competitive when compared with recent TiO_2-based systems reported in the literature. For instance, a TiO_2/NiFe-LDH heterostructure reported by Liu et al. (2023) exhibited a photocurrent density of 0.0187 A/cm² at 0.6 V vs. RHE under AM 1.5G illumination, highlighting the efficacy of MnO_2 modification in this study. These results support the effectiveness of the polynomial-optimized calcination strategy in enhancing the photoelectrochemical performance of TiO_2-based photoanodes.

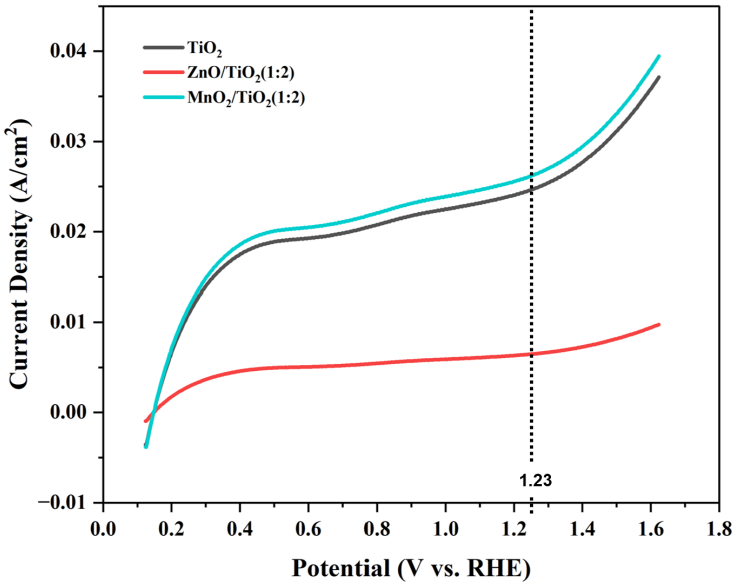

Figure 4 LSV plots for TiO_2, ZnO/TiO_2 (1:2), and MnO_2/TiO_2 (1:2) after 2h illumination.

The relatively poor PEC performance of ZnO/TiO_2 (1:2) compared to pristine TiO_2 may be attributed to the electronic characteristics of ZnO. The fulfilled d-orbitals of Zn(II) ions may result in a stable, less reactive state that does not actively engage in electron transfer. This reduced reactivity hampers efficient charge separation and transfer, as reflected by the lower photocurrent density and higher charge transfer resistance observed in ZnO/TiO_2 compared to pristine TiO_2. The enhanced performance of the MnO_2/TiO_2 (1:2) photoanode can be attributed to the formation of a heterojunction. The incorporation of MnO_2 into TiO_2 is believed to enhance photoelectrochemical activity by improving charge separation and modifying the band gap. Medhi et al. (2020) emphasized that interstitial doping of transition metals with partially filled d-orbitals into d^0- or d^{10}-based oxides is an effective strategy for narrowing band gaps. However, introducing transition metal cations with partially filled d-orbitals into photocatalytic materials may also lead to inefficient photo-responses.

In principle, LSV measurements provide key insights into the PEC performance of TiO_2-based photoanodes by illustrating the relationship between applied potential and current density under both dark and illuminated conditions. As shown in Figure 5(a), upon light irradiation, pristine TiO_2 demonstrates a noticeable increase in photocurrent, indicative of efficient photogeneration of charge carriers, although this enhancement is constrained by its wide bandgap (~3.2 eV), which limits absorption to the ultraviolet (UV) region, accounting for only ~5% of the solar spectrum. Notably, the ZnO/TiO_2 (1:2) composite in Figure 5(b) exhibits improved charge separation efficiency due to favorable band alignment that facilitates interfacial electron transfer and suppresses recombination losses. MnO/TiO_2 (1:2), however, achieves even greater photocurrent densities in Figure 5(c), benefitting from MnO's narrower bandgap (~2.6 eV) and a conduction band minimum (CBM) at approximately -0.25 V vs. RHE, which supports thermodynamically favorable proton reduction and accelerated hydrogen evolution reaction (HER) kinetics (Abdelfattah & El-Shamy, 2024; Das et al., 2024).

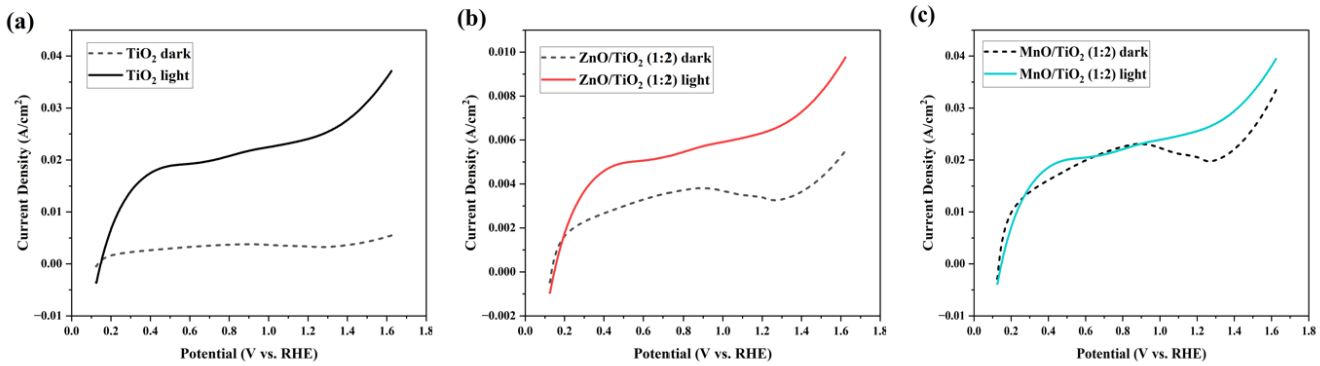

Figure 5 LSV plots comparing photocurrent density between dark conditions and after 2h illumination for (a) TiO_2, (b) ZnO/TiO_2 (1:2) and (c) MnO_2/TiO_2 (1:2).

Figure 6 displays the Nyquist plots of TiO_2, ZnO/TiO_2 (1:2), and MnO_2/TiO_2 (1:2) photoanodes, measured and fitted after 2h of illumination. The extracted charge transfer resistance (R_{ct}) values show a distinct trend in interfacial kinetics. Among the samples, MnO_2/TiO_2 (1:2) exhibits the lowest R_{ct} at 9.76 Ω, which corresponds to the highest photocurrent density observed in LSV measurements (Figure 5(c)). This enhanced performance is attributed to the effective heterojunction formed between MnO_2 and TiO_2, which facilitates efficient charge separation and suppresses electron-hole recombination. In comparison, pristine TiO_2 shows a moderate R_{ct} of 16.20 Ω (Figure 5(a)), reflecting its intrinsic limitations such as a wide bandgap (~3.2 eV) that restricts absorption to the UV region and promotes a higher recombination rate (Taneja et al, 2024). Meanwhile, the ZnO/TiO_2 (1:2) composite displays the highest R_{ct} of 17.93 Ω (Figure 5(b)). and the lowest photocurrent density among the modified photoanodes, likely due to grain boundary effects that hinder electron transport despite improved light absorption from ZnO's narrower bandgap (~3.0 eV).

The trend in R_{ct} values align inversely with the photocurrent response, highlighting the critical role of charge transfer dynamics in determining photoelectrochemical performance. A lower R_{ct}, as seen in MnO_2/TiO_2, signifies improved interfacial charge transport and catalytic activity, leading to more efficient HER kinetics. In contrast, a higher R_{ct}, as observed in ZnO/TiO_2, suggests kinetic bottlenecks such as poor interfacial conductivity and restricted electron mobility. This strong correlation between electrochemical impedance spectroscopy (EIS) and LSV results underscores the importance of interface engineering in optimizing photoanode design for enhanced solar-driven water splitting efficiency.

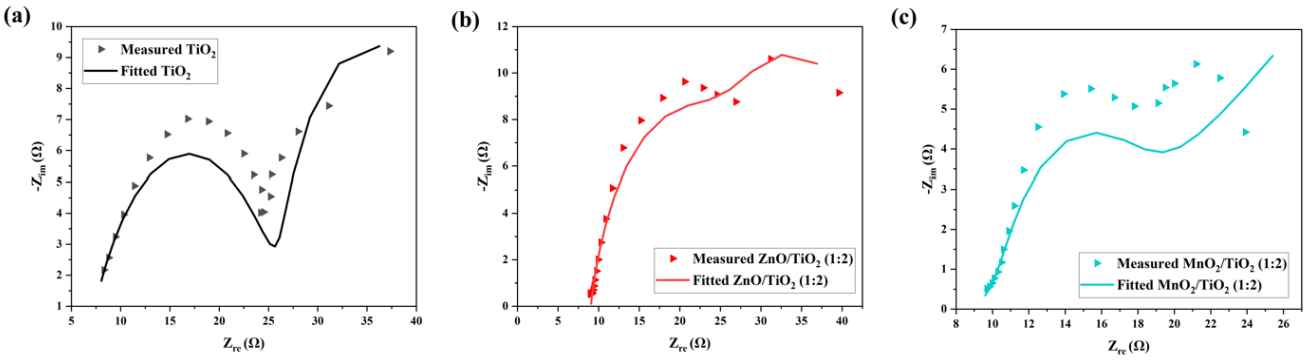

Figure 6 Nyquist plot of (a) TiO_2, (b) ZnO/TiO_2 (1:2) and (c) MnO_2/TiO_2 (1:2).

The optimization of the calcination temperature, guided by polynomial fitting, plays a pivotal role in the formation of a well-defined heterojunction between MnO_2 and TiO_2. This tailored calcination process not only improves the material's structural integrity but also optimizes the interfacial properties, leading to more efficient charge separation and reduced electron-hole recombination. On the other hand, the higher R_{ct} values observed for pure TiO_2 and ZnO/TiO_2 (1:2) reflect suboptimal charge transport properties, potentially exacerbated by less effective calcination conditions or inadequate heterojunction formation. As a result, the polynomial-optimized calcination temperature plays an important role in increasing the photoanode's overall performance by optimizing charge transfer dynamics, which contributes to the efficient solar-driven water splitting process.

4.0 CONCLUSION

This study demonstrates the successful integration of data-driven modeling with materials synthesis to optimize the calcination temperature of TiO_2-based photoanodes for enhanced PEC water splitting. Using a fifth-order polynomial fitting model, an optimal calcination temperature of 550 °C was identified, resulting in improved crystallinity and phase purity in TiO_2 and its composites with ZnO and MnO_2. X-ray diffraction analyses confirmed the formation of anatase TiO_2, wurtzite ZnO, and β-MnO_2 phases, while shifts in d-spacing and increases in crystallite size indicated the formation of heterojunctions. Among the photoanodes studied, MnO_2/TiO_2 (1:2) exhibited the highest photocurrent density (0.02052 A cm^{-2}) and the lowest charge transfer resistance (9.76 Ω), validating the effectiveness of the polynomial-optimized calcination approach. The enhanced photoresponse of MnO_2/TiO_2 (1:2) is attributed to improved interfacial charge dynamics facilitated by heterojunction formation, which enhances charge separation and suppresses recombination. In contrast, ZnO/TiO_2 (1:2) exhibited higher R_{ct} and lower photocurrent density due to its larger crystallite size and the presence of insulating grain boundaries that hinder electron transport. These findings emphasize the critical role of calcination temperature in tailoring the structural and electrochemical properties of photoanodes. Overall, this work presents a rational and reproducible strategy for enhancing photoanode performance through predictive modeling and controlled thermal processing, offering a promising pathway for advancing solar-driven hydrogen production technologies.

Acknowledgment

The authors acknowledge the financial support from the Ministry of Higher Education Malaysia under the Fundamental Research Grant Scheme (FRGS) No. FRGS/1/2023/STG04/UTM/02/1 at cost center no.: R.J130000.7854.5F647

References

[1] Jang, Y. J., Kim, H. G., & Choi, W. (2016). Revisiting the Role of Photogenerated Charge Carriers in Heterogeneous Photocatalysis: A Perspective Based on Ultrahigh-Resolution Photoemission and Transient Absorption Spectroscopies. *Chemical Society Reviews*, *45*(12), 3015–3034. https://doi.org/10.1039/C5CS00848F

[2] Xu, Y., Zhang, X., Li, Q., & Liu, S. (2021). Advances in Bandgap Engineering of TiO_2-Based Materials for Enhanced Photoelectrochemical Water Splitting. *Applied Surface Science*, *558*, 149979. https://doi.org/10.1016/j.apsusc.2021.149979

[3] Thabet, N., Ahmed, A., & Yusof, M. (2024). Enhanced Photoelectrochemical Hydrogen Production via Transition Metal Co-Catalyst Decorated TiO_2 Nanostructures. *Scientific Reports, 14*(1), Article 11234. https://doi.org/10.1038/s41598-024-11234-x

[4] Jiang, C., Moniz, S. J. A., Wang, A., Zhang, T., & Tang, J. (2016). Photoelectrochemical Devices for Solar Water Splitting – Materials and Challenges. Chemical Society Reviews, 46(15), 4645–4660. https://doi.org/10.1039/C6CS00306K

[5] Wang, Y., Zhang, K., Wang, X., Liu, Q., & Zhang, L. (2021). Calcination Temperature Dependent Photocatalytic Activity and Physicochemical Properties of TiO_2 Nanoparticles. *Materials Science in Semiconductor Processing*, *131*, 105830. https://doi.org/10.1016/j.mssp.2021.105830

[6] Oral, B., Can, E., & Yildirim, R. (2022). Analysis of Photoelectrochemical Water Splitting Using Machine Learning. *International Journal of Hydrogen Energy, 47*(45), 19633–19654. https://doi.org/10.1016/j.ijhydene.2022.01.011

[7] Sun, Y., Wang, Y., Li, Y., Zhang, X., & Liu, H. (2020). One-step Hydrothermal Preparation and Characterization of ZnO–TiO_2 Nanocomposites for Photocatalytic Activity. *Materials Research Express*, 7(9), 095004. https://doi.org/10.1088/2053-1591/abaea4

[8] Alonizan, N., Rabaoui, S., Omri, K., & Qindeel, R. (2018). Microstructure and Luminescence Properties of ZnO:Mn Nanoparticles and ZnO:Mn/TiO_2 Nanocomposite Synthesized by A Two-Step Chemical Method. *Applied Physics A*, 124(9), 710. https://doi.org/10.1007/s00339-018-2127-y

[9] Lai, M. T. L., Lee, K. M., Yang, T. C. K., Lai, C. W., Chen, C.-Y., Johan, M. R., & Juan, J. C. (2023). Highly Effective Interlayer Expanded MoS_2 Coupled with Bi_2WO_6 as P-N Heterojunction Photocatalyst for Photodegradation of Organic Dye Under LED White Light. *Journal of Alloys and Compounds*, 953. https://doi.org/10.1016/j.jallcom.2023.169834

[10] Manna, S., Satpati, A. K., Patra, C. N., & Tyagi, A. K. (2024). Enhancing the PEC Eefficiency in the Perspective of Crystal Facet Engineering and Modulation of Surfaces. *ACS Omega, 9*(6), 6128–6146. https://doi.org/10.1021/acsomega.3c07867

[11] Liu, S., Tang, Y., Guo, C., Liu, Y., & Tang, Z. (2023). Heterostructure of NiFe@NiCr-LDH for Active and Durable Oxygen Evolution Reactions in Alkaline Media. *Materials, 16*(8), 2968. https://doi.org/10.3390/ma16082968

[12] Medhi, R., Marquez, M. D., & Lee, T. R. (2020). Visible-light-active Doped Metal Oxide Nanoparticles: Review of Their Synthesis, Properties, and Applications. *ACS Applied Nano Materials*, 3(7), 6156–6185. https://doi.org/10.1021/acsanm.0c01035

[13] Abdelfattah I & El-Shamy AM (2024). A Comparative Study for Optimizing Photocatalytic Activity of TiO_2-based Composites with ZrO_2, ZnO, Ta_2O_5, SnO, Fe_2O_3, and CuO Additives. *Scientific Reports*. 14(1), 27175. https://doi.org/10.1038/s41598-024-77752-5

[14] Das, A., Liu, D., Wu, Y., Abzakh, B. A., Kazakova, E. A., Vasenko, A. S., & Prezhdo, O. V. (2024). Origin of the Improved Photoelectrochemical and Photocatalytic Activity in a ZnO-TiO_2 Nanohybrid Revealed by Experimental and Density Functional Theory Studies. *The Journal of Physical Chemistry Letters*, 15(29), 7524-7532. https://doi/full/10.1021/acs.jpclett.4c01641

[15] Taneja, Y., Dube, D., & Singh, R. (2024). Recent Advances in Elemental Doping and Simulation Techniques:Improving Structural, Photophysical and Electronic Properties of Titanium Oxide. *Journal of Materials Chemistry C*. 12, 14774-14808.https://doi.org/10.1039/D4TC02031F